
RESEARCH ARTICLE

Quarterly Journal of the Royal Meteorological Society

The effect of ambient shear on coherent boundary layer structures

Leif Denby¹ | Steven J. Böing¹ | Douglas J. Parker¹ |
Andrew N. Ross¹ | Steven M. Tobias²

¹School of Earth and Environment,
University of Leeds

²School of Mathematics, University of
Leeds

Correspondence

Leif Denby, Institute for Climate and
Atmospheric Science, School of Earth and
Environment, University of Leeds, Leeds,
LS2 9JT, United Kingdom
Email: l.c.denby@leeds.ac.uk

Funding information

Met Office/NERC Grant NE/N013840/1

This paper presents two techniques for characterisation of cloud-feeding coherent boundary layer structures through analysis of large-eddy simulations of shallow cumulus clouds, contrasting conditions with and without ambient shear. The first technique is a generalisation of the two-point correlation function where the correlation length-scale as well as orientation can be extracted. The second technique consists of decomposing the boundary layer air into individual coherent structures and thereafter characterising each object by size, orientation and moisture flux carried. Using these techniques it is found that the majority of vertical moisture flux is carried by plume-like structures with volume scaling with the height of the boundary layer. This plume-like structure is in apparent contrast with the assumptions of some modelling systems, that fluxes are carried by thermals, and therefore the conclusions are significant to parametrisation development for weather and climate models. The elongation and orientation of boundary layer structures caused by the introduction of ambient shear is also quantified, demonstrating the general applicability of the techniques for future study of other boundary layer patterns.

Keywords – moist convection, coherent structures, convective triggering

1 | INTRODUCTION

Coherent boundary layer structures carry perturbations of temperature, moisture and vertical velocity necessary to trigger convective clouds by overcoming the boundary layer top inversion in a conditionally unstable atmosphere. However, the degree to which the spatial distribution, morphology and perturbations carried by the coherent structures affect how clouds form is currently uncertain, as is which external drivers affect these properties of the coherent structures. To study comprehensively the formation of clouds from coherent boundary layer structures we must first be able to identify and measure the properties of these structures, which is the aim of this paper.

Coherent structures in the boundary layer carry so-called non-local (cannot simply be calculated from local scalar values) counter-gradient transport in the boundary layer (Deardorff, 1966), providing transport against the vertical mean gradient of moisture and heat (in contrast to smaller turbulent eddies doing down-gradient, diffusive, transport). Owing to the limited resolution available in Global Circulation Models and Numerical Weather Prediction models, it is necessary to parameterise the unresolved sub-grid processes that provide vertical transport and lead to convective cloud formation. The development of parameterisations of non-local transport has been key to improving boundary-layer parameterisations (Holtslag and Moeng, 1991; Brown and Grant, 1997). Over the past two decades, the Eddy-Diffusivity Mass-Flux (EDMF) approach to boundary-layer parameterisation (e.g. Siebesma et al., 2007) has become popular: in this approach, local turbulent transport and transport by coherent structures (leading to the formation of convective clouds) are modelled separately. However, our current limited knowledge of the nature of these coherent structures limits our ability to refine models of the non-local transport, and thus in representing the genesis (formation) of convective clouds in weather and climate simulations.

As well as influencing the formation of individual clouds, these structures capture the convective state of the atmosphere, through their spatial organisation and by persisting sub-grid length-scales of motion over time, in a poorly understood coupling between the sub-cloud and cloud layer. Representation of these sub-grid forms of organisation (a form of convective "memory") are largely absent in contemporary convection parameterisations, however the importance of convective organisation in affecting, for example, the radiative properties of the atmosphere, and the impact of limited representation of these processes in models, is becoming increasingly clear (Bony et al., 2017).

Prior work has focused primarily on measuring coherence in the boundary layer as a whole, not looking at the properties of individual coherent structures, but instead producing bulk length-scale estimates using spectral peaks in the autocorrelation and covariance spectrum to measure spatial and angular coherence (in the horizontal plane). Jonker et al. (1999) found in cloud-free Large-Eddy Simulations (LES) that the shortest correlation length-scale exists in vertical velocity on the order of the boundary-layer depth, whereas the buoyancy providing field (potential temperature θ for dry LES, virtual potential temperature θ_v when water vapour is included) typically attains larger steady-state length-scales (Jonker et al., 1999; Salesky et al., 2017; de Roode et al., 2004). De Roode et al. (2004) in addition found that for passive tracers in dry and stratocumulus topped boundary layers the vertical profile of horizontal length-scales is determined by the surface to boundary-layer top buoyancy flux ratio $r = \frac{w'\theta'_{v,T}}{w'\theta'_{v,0}}$, with minimum length-scales attained when this ratio was $r \approx -0.2$ for dry convection (which is the classical buoyancy flux-ratio scale found for dry convective boundary layers) and $r \approx -1$ for the stratocumulus case.

In simulations where clouds are present the picture becomes more complicated for the dynamic scalars (Schumann and Moeng, 1991; de Roode et al., 2004), apart from vertical velocity which stays largely unchanged (restricted dynamically by the boundary-layer depth). The buoyancy (θ_v) no longer necessarily reaches a steady-state length-scale profile, and water-vapour and potential temperature produce meso-scale variability (which appear to cancel in their contributions to θ_v). The length-scale characteristics found in LES have been supported through similar analysis of observations (Nicholls and Lemone, 1980; Lenschow and Sun, 2007), with the relative scales of q and θ changing with Bowen ratio,

producing narrower scales for the scalar dominating buoyancy. Identifying and characterising coherent structures in observations Schumann and Moeng (1991) found that coherence length-scale typically peaks mid boundary-layer, where the number of structures reaches a minimum. Miao et al. (2006) found the plume spacing and width to be $0.7h_{BL}$ and $0.2h_{BL}$ respectively mid boundary-layer.

In place of studying correlation in inverse distance (or wave-length) space, the present work studies correlation in real space using cumulants (see history and review by Lauritzen, 2007). Cumulants have been applied by Lohou et al. (2000) to study thermals in a daytime boundary layer with weak wind shear over land, and characterise the influence of anisotropy on vertical transport. Schmidt and Schumann (1989) used cumulants to study coherence in the vertical rather than the horizontal plane, and identified both large-scale plumes and transient thermals in a convective boundary layer. They have also been used to expand the prognostic equations (Ait-Chaalal et al., 2016). In modelling by Lohou et al. (2000) and Schmidt and Schumann (1989) correlation is studied in real space, rather than inverse distance, or wave-length space. In this work we develop this technique further by utilising cumulants and producing vertical profiles of integral length-scale and orientation of coherence in real space.

With respect to identifying coherent structures in the boundary layer prior work focused on using limit values on vertical velocity or water vapour concentration (either separately or in combination) to define object masks (Berg and Stull, 2004; Grant and Brown, 1999; Nicholls and Lemone, 1980; Schumann and Moeng, 1991). More recently Efstathiou et al. (2020) developed a masking technique to maximise the vertical transport carried by the selected region of the boundary layer. Couvreux et al. (2010) noted that object masks based on the physical fields (vertical velocity, water vapour, temperature) had the drawback that they poorly capture transport through the boundary layer top inversion and into the cloud-layer, and proposed a technique based on a surface-released decaying passive tracer to track the rising boundary layer structures. This tracer technique has been used to identify coherent structures in cloudy boundary layers (Dawe and Austin, 2012; Park et al., 2016; Brient et al., 2019). The current work uses the tracer in combination with the object-splitting technique described in Park et al. (2018) to identify individual structures that are characterised by a prominent local maximum of the vertical velocity in the boundary layer.

The aim of this paper is to demonstrate the use of new techniques to identify and characterise coherent structures in the boundary layer and to provide the means to separate out and quantify the non-local transport done by coherent boundary layer structures. The identification method presented here seeks to identify coherent structures with properties necessary to trigger clouds without formulating constraints on the thermodynamic and dynamic properties, and instead utilise a passive tracer advected with the field. The spatial form and orientation of these coherent structures are quantified so that the characteristic properties of structures which carry the majority of the vertical (cloud-triggering) transport may be identified. Knowing the form and scales of cloud-triggering boundary-layer structures will inform development of new models of convective triggering and provides a framework for studying the transient development of scales of organisation.

As a means of investigating the extent to which the methods discussed herein are able to unpick and quantify boundary layer transport and its influence on clouds in different environmental conditions, we will use two simulations of shallow convection, with and without shear, as a demonstration of large-scale influence on coherent boundary layer structures and convective clouds. The modelling setup for the simulations are discussed in Sec. 2. The methods used to identify coherent boundary layer structures and quantify their properties will be discussed in Sec. 3. Finally the application of these methods will be shown in Sec. 4 and a discussion of this analysis will be given in Sec. 5.

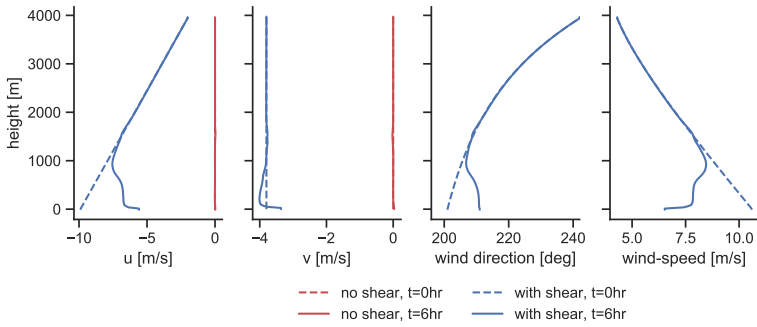


FIGURE 1 Vertical profiles of horizontal mean wind at times $t = 0$ h and $t = 6$ h in meridional (v) and zonal (u) directions together with wind direction ϕ (measured from x -axis) for cases with and without shear. Mean wind direction in sub-cloud layer after $t = 6$ h is at $\phi \approx 210^\circ$ in simulation with shear.

2 | MODELLING SETUP

Simulations were carried out with the non-hydrostatic UCLA-LES Large-Eddy Simulations model (Stevens et al., 2005) with two-moment warm-rain microphysics scheme (Stevens and Seifert, 2008) on a $40 \text{ km} \times 40 \text{ km} \times 4 \text{ km}$ double-periodic domain with an isotropic grid-spacing of $(\Delta x, \Delta y, \Delta z) = (25, 25, 25) \text{ m}$.

The simulation setup is based on the Rain in Cumulus over the Ocean (RICO) field study (Rauber et al., 2007) and associated LES model inter-comparison study (VanZanten et al., 2011). The RICO setup is characterised by shallow cumuli developing from moisture-dominated fluxes from the ocean surface, with the clouds constrained in growth by a prescribed large-scale subsidence aloft and large-scale advection of moisture out of the domain. In the original inter-comparison study, the simulation settles into a quasi-steady state after a short (≈ 2 h) rapid response to the initial condition, after which convection slowly (over ≈ 20 h) aggregates into larger cloud clusters by precipitation-induced cold pools. As the process leading to formation of these cloud clusters is not the focus of this study, we will be considering only the stage of cloud development before these large clusters have developed (here using $t = 6$ h).

In this work there are two key differences to the original RICO setup as published in Seifert et al. (2015). Firstly, in order to study the effect of ambient wind-shear on the coherent boundary layer structures, two simulations were run, one with and one without shear (see profiles in Fig. 1). In the former the wind-profile from RICO was left unchanged and in the latter the meridional and zonal wind components were set to zero. Secondly, because the near-surface horizontal velocity differs between the two simulations, the bulk aerodynamic parameterisation of surface flux was replaced with a fixed sensible ($F_s = 7 \text{ W/m}^2$) and latent heat flux ($F_v = 150 \text{ W/m}^2$) so that the two conditions have the same fluxes provided from the surface. The surface flux values were estimated from the original RICO simulation once near-equilibrium conditions have been reached (at $t \approx 6$ h).

As seen in the horizontal cross-sections of vertical velocity in Fig. 2, the presence of ambient shear causes both boundary-layer structures and clouds to become organised into elongated structures instead of convective cells. This is noticeable through the elongated line-like regions of high vertical velocity in simulations with shear, causing the clouds (cloud-base is at $z \approx 650$ m) to organise into structures resembling *cloud streets* instead of (as in the case without shear) at the nodes of boundary-layer convective cells. The development of cloud streets under conditions with ambient shear is consistent with prior studies (see reviews by Etling and Brown, 1993; Young et al., 2002), as is the presence of sheet-like coherent structures attached to the surface extending into the bulk of the boundary layer (as in Khanna and Brasseur, 1998).

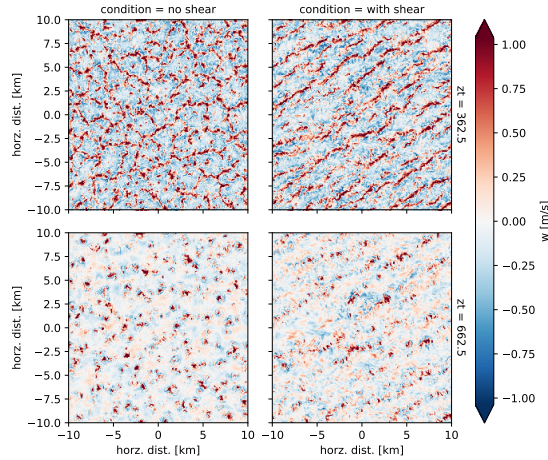


FIGURE 2 Horizontal cross-sections of vertical velocity through the boundary-layer middle ($z \approx 362.5$ m, top) and at cloud-base height ($z \approx 662.5$ m, bottom) for simulations with shear (right) and without (left). The presence of ambient shear is seen to clearly break the geometry of convective cells and create elongated coherent boundary structures.

3 | METHODS

Before the properties of coherent boundary layer structures that trigger clouds can be measured, it is necessary to define exactly what we mean by a coherent structure. In contrast to the cloud layer, where we can define a coherent structure purely on the concentration of water droplets, in the boundary layer there are at least three scalar fields that carry the perturbation that eventually triggers a cloud: moisture, temperature and vertical velocity.

We first investigate the length-scales of variability in these fields as a bulk-property of the fluid. If these fields were to vary over similar length-scales it would be relatively straightforward to define threshold criteria on either of the scalar fields that would apply to all fields. Unfortunately this is not the case (section 3.1) and so we instead develop a method which identifies air with properties similar to that which triggers convective clouds (section 3.2.1), by tracking air entering newly-formed convective clouds.

3.1 | Characteristic length-scales - cumulant analysis

As an alternative to moments, cumulants provide a means to summarise the statistical correlation between one or more variables (Lauritzen, 2007). Similarly to Tobias and Marston (2017), where cumulants were used to identify and measure coherent structures in 3D rotating Couette flow, we here utilise the second cumulant (two-point correlation function), which for fields ψ and φ at height z (here $z_1 = z_2 = z$ in contrast to Tobias and Marston, 2017) is given by

$$c_{\psi\varphi}(\xi, \nu, z) = \frac{1}{L_x L_y} \int_0^{L_x} \int_0^{L_y} \psi'(x, y, z) \varphi'(x + \xi, y + \nu, z) dx dy,$$

where ψ' and φ' are deviations from the horizontal mean of ψ and φ respectively, and L_x and L_y are the lengths of the domain in the x - and y -direction. The positions are wrapped around in the x - and y -direction exploiting the periodic

boundary conditions of the simulation.

An example of this method applied to the spatial correlation of vertical velocity ($\psi = w$) and water vapour ($\varphi = q_v$) in the middle of the boundary layer in a simulation with ambient shear is shown in Fig. 3. In cases such as this where an external forcing is causing boundary-layer and cloud structures to develop in a preferential direction, the characteristic length-scale will be longer in this direction. To quantify this asymmetry we identify a *principal* and *perpendicular* direction of coherence (measured in terms of the angles θ_p and θ_\perp) of the central part of the cumulant. This central part $\hat{c}_{\psi\varphi}$ is defined as the connected region at the origin with the same sign as at the origin of the cumulant $c_{\psi\varphi}$. Treating $\hat{c}_{\psi\varphi}$ as a 2D mass-distribution, we then estimate the orientation angle as the principal axis (eigenvector with largest eigenvalue) of the moment of inertia tensor:

$$\bar{\bar{I}} = \begin{bmatrix} \int \hat{c}_{\psi\varphi}(\xi, \nu) \nu^2 d\xi d\nu & \int \hat{c}_{\psi\varphi}(\xi, \nu) \xi \nu d\xi d\nu \\ \int \hat{c}_{\psi\varphi}(\xi, \nu) \xi \nu d\xi d\nu & \int \hat{c}_{\psi\varphi}(\xi, \nu) \xi^2 d\xi d\nu \end{bmatrix}. \quad (1)$$

The cumulant can then be sampled in this horizontal plane along the principal and perpendicular directions of coherence (as seen in Fig. 3 right) so that the coherence can be quantified in these directions. The presence of ambient shear is for example seen to cause elongation in the direction of the ambient wind (this will be discussed in detail in section 4.1).

Once the direction of principal coherence (θ_p) has been identified, a characteristic length-scale (L_p) of coherence may be estimated in this direction and similarly in the perpendicular direction (L_\perp). These length-scales are computed through a cumulant-weighted integral of distance ($l = \sqrt{\xi^2 + \nu^2}$) from the cumulant origin:

$$L_\delta^{\psi,\varphi} = \frac{\int_\infty^\infty l \hat{c}_{\psi,\varphi}^\delta(l) dl}{\int_\infty^\infty \hat{c}_{\psi,\varphi}^\delta(l) dl}, \quad (2)$$

where $\delta \in [p, \perp]$ (for either the principal or perpendicular length-scale), with the cumulant along a particular direction given by

$$\hat{c}_{\psi,\varphi}^\delta(l) = \hat{c}_{\psi,\varphi}(\xi=l \cos(\theta_\delta), \nu=l \sin(\theta_\delta)) \quad (3)$$

evaluated at an arbitrary point using piece-wise linear interpolation.

As will be discussed in section 4.1, the presence of ambient shear creates a marked elongation of this coherence length-scale across all scalar fields, and this direction coincides with ambient wind direction.

As well as providing a means to quantify the length-scale of correlation (and thus a single characteristic length-scale for all coherent boundary layer structures), the shape of the cumulant can provide insight into the dynamical structure of coherent structures by quantifying the relative spatial distribution of different scalar fields. This is possible by studying two different aspects of the cumulant produced from two different fields, specifically the offset of the cumulant peak value from the origin and the skewness of the distribution around the origin. An offset of the cumulant from the origin indicates that the extreme values of two different scalar fields are located spatially offset from each other and would suggest something is driving a separation between two fields. Similarly, skewness in the cumulant distribution indicates that the two different scalar fields have differently spatially skewed distributions, e.g one field may appear spatially Gaussian, but another may be skewed relative to this. The corollary to this is that a 2nd cumulant, between two different scalar fields, which is centered on and symmetric around the origin, indicates that these two fields on average are

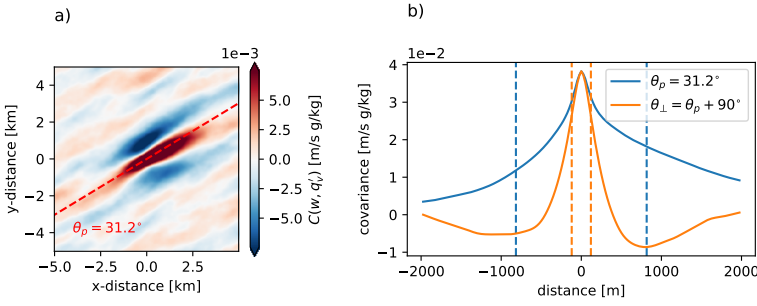


FIGURE 3 a) Cumulant of vertical velocity and water vapour (i.e. the horizontal moisture flux) in horizontal plane at $z = 300$ m with principal direction of coherence identified by the red dashed line, and b) the same cumulant sampled along (in blue) and perpendicular (in orange) to the principal axis with characteristic (integral) width indicated with vertical lines. The elongated nature of the coherence as seen on the left is quantified by a significantly larger (≈ 1500 m vs ≈ 500 m) characteristic length along the direction of shear.

spatially distributed identically (in terms of skewness) around their respective peak values and their peak values are, on average, co-located.

3.2 | Object-based analysis

To gain a more comprehensive understanding of transport by coherent structures in the boundary layer, we transition from looking at the boundary layer air in a bulk sense, to studying transport by individual coherent structures that may trigger clouds. This requires identifying the regions of the boundary layer that contribute to transport into convective clouds, splitting these regions into individual coherent structures and finally formulating methods to quantify the properties of these structures.

3.2.1 | Object identification

To quantify the characteristic properties of individual coherent structures carrying out vertical transport, these structures must first be identified. This was achieved by first producing a 3D mask to pick out the part of the atmosphere thought to contain coherent structures, and thereafter splitting this mask into individual 3D objects.

The 3D mask was produced from the concentration of a passive tracer (ϕ) decaying with a time-scale τ , which was released from the surface (as first used in Couvreux et al., 2010). Specifically the time evolution of the tracer is given by

$$\frac{\partial \phi}{\partial t} = -\frac{\phi}{\tau}. \quad (4)$$

The decay time-scale was set to $\tau = 15$ min in this study as this represents the typical overturning time-scale of boundary-layer eddies in the simulations used (see appendix A).

From the scalar ϕ a mask is created using its standard deviation in a horizontal cross-section ($\sigma_\phi(z)$) and its local deviation from the horizontal mean ($\phi'(x, y, z) = \phi(x, y, z) - \bar{\phi}(z)$) by requiring that the local deviation is n standard

deviations from the mean, i.e. the mask $m(x, y, z)$ is given by

$$m(x, y, z) = \begin{cases} 1 & \text{if } \phi'(x, y, z) > n \sigma_{\phi}(x, y, z), \\ 0 & \text{otherwise} \end{cases} \quad (5)$$

here $n = 2$ was used as this was found to produce closest agreement between the properties of air entering clouds and those identified to belong to coherent structures (see section 4.2). The choice of decay time-scale and limit value for n is similar to those ($\tau = 15$ min and $n = 2.5$) identified by Chinita et al. (2018) to be optimal when studying shallow moist convection in the BOMEX (Barbados Oceanographic and Meteorological Experiment) case (Siebesma et al., 2003).

The constructed 3D mask was observed to identify boundary layer air with thermodynamic properties similar to air entering into recently formed clouds (see section 4.3 for details), making it a suitable method to distinguish vertical transport by local diffusive mixing (small eddies) from transport by larger non-local eddies carrying fluxes leading to cloud-formation.

Using the method of Park et al. (2018), individual three-dimensional objects were identified from the mask by first labelling contiguous regions of the mask as individual *proto-objects* and further splitting these proto-objects where they were deemed to be comprised of individual objects, for example as two individual rising thermals which were touching.

The sub-division of the proto-objects was done by first creating *fragments* from each proto-object and merging these fragments into individual objects. The identification and merging of fragments was done through the use of a second scalar field (γ), here vertical velocity ($\gamma = w$) with the aim to identify individual rising structures. The fragments were created by assigning a unique label to each cell within a proto-object which had a local maximum in γ , and associating the remaining proto-object cells to these labels by iteratively copying the labels of neighbouring cells in the direction of steepest local gradient in γ . Neighbouring fragments were then merged, if for two fragments the following criterion was satisfied

$$\frac{\gamma_l - \gamma_c}{\gamma_l - \gamma_m} \leq f, \quad (6)$$

where γ_l is the smallest value of the two fragment local maxima, γ_c the lowest value along their interface (the "col"), γ_m is the minimum value encountered in either of the two fragments and f is a tunable parameter controlling how shallow the col must be for two fragments to be merged. Here $f = 0.7$ was used as in Park et al. (2018).

To measure the thermodynamic properties of air causing the formation of clouds, individual clouds were identified from 2D column-integrated liquid water path (m_{IWP}) with a threshold value of $m_{IWP} > 0.01$ kg/m² and tracked by spatial overlap in consecutive time-steps using the method detailed in Heus and Seifert (2013). This method identifies *active* clouds as ones with at least one buoyant core (identified from the virtual potential temperature θ_v) and *passive* clouds as those without a buoyant core. In addition, this cloud-tracking method splits clouds with multiple buoyant cores into smaller sub-clouds with the non-buoyant regions defined as *outflow*. In this work we only consider the properties of air entering single-core *active* clouds as these are likely to have the strongest and clearest connection to boundary layer variations. To facilitate selecting clouds which recently formed we also keep track of the age of each cloud (t_{age}) by storing the time of appearance for each tracked cloud.

3.2.2 | Object characterisation

Once individual 3D coherent structures have been identified, a method is needed to calculate characteristic properties of these objects. Here we detail techniques to compute characteristic length-scales and orientation of each coherent

structure.

Topological measures - Minkowski functionals

Instead of attempting to fit a parameterised shape (for example an ellipsoid) to each object with the intention of estimating an object's scale (length, width and thickness), we instead calculate a set of characteristic scales using the so-called *Minkowski functionals* (Minkowski, 1903) that measure the topology of arbitrary structures in N -dimensional space (see review by Mecke (2000) for details). These have been used in other physical applications to characterise for example dissipative structures in magnetohydrodynamic turbulence (Zhdankin et al., 2014), galaxy distribution (Schmalzing and Buchert, 1997) and cosmological structure formation (Sahni et al., 1998; Schmalzing et al., 1999). In three dimensions the Minkowski functionals are

$$V_0 = V = \int dV, \quad (7)$$

$$V_1 = \frac{A}{6} = \frac{1}{6} \int dS, \quad (8)$$

$$V_2 = \frac{H}{3\pi} = -\frac{1}{6\pi} \int \nabla \cdot \hat{\mathbf{n}} dS = \frac{1}{6\pi} \int (\kappa_1 + \kappa_2) dS, \quad (9)$$

$$V_3 = \frac{1}{4\pi} \int (\kappa_1 \kappa_2) dS, \quad (10)$$

where $\hat{\mathbf{n}}$ is the surface normal, and κ_1, κ_2 are the maximum and minimum local curvature. To evaluate these integrals numerically on the discrete output from the large-eddy simulations, we use Crofton's formula (see Appendix B), which provides discrete approximations for terms (for example the surface normal) which are otherwise difficult to evaluate on objects constructed from individual cubic volumes of the simulations underlying grid. For reference, the Minkowski functionals for a parameterised spheroid and ellipsoid will be shown, using the analytical expressions (where available, and otherwise numerical integration) for surface area and mean curvature given in Schmalzing et al. (1999) and Poelaert et al. (2011).

From these functionals a characteristic *length* (L_m), *width* (W_m) and *thickness* (T_m) can be calculated as

$$L_m = \frac{3V_2}{4V_3}, W_m = \frac{2V_1}{\pi V_2}, T_m = \frac{V_0}{2V_1}, \quad (11)$$

where the normalisation is such that all of these measures equal the radius when applied to a sphere. These may be further summarised by computing the *filamentarity* (F_m) and *planarity* (P_m)

$$F_m = \frac{L_m - W_m}{L_m + W_m}, P_m = \frac{W_m - T_m}{W_m + T_m}, \quad (12)$$

which in turn indicate whether an object is more *stick-like* (large filamentarity) or *pancake-like* (large planarity).

The Minkowski functionals thus enable the quantification of an object's shape, making it possible to, for example, investigate whether the objects that are the primary contributors to vertical transport have a characteristic shape, which is key in deciding how to model this transport.

To provide a reference for the range of values which may be expected for coherent structures in the atmospheric boundary layer, Fig. 4 is a filamentarity vs planarity plot for a number of synthetically created, numerically integrated, sheared and stretched spheroids. The centerline length was kept constant across all shapes while varying the width and shearing distance. Each data point is marked by an outline of the shape's structure by plotting the vertical cross-section through each shape's symmetry plane. As a means of reference for the numerically integrated shapes the analytical

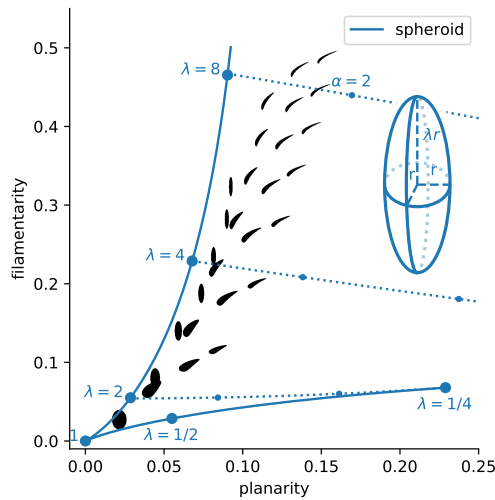


FIGURE 4 Filamentarity vs planarity plot for synthetically created 3D thermal structures with centerline length 500 m and varying shear and distance. For each structure the data point is marked with a vertical cross-section. For reference the analytical solution for a spheroid with varying major to minor-axis ratio (λ) is included in solid blue together with reference lines for deforming a spheroid through a general ellipsoid with fixed major axis and volume while changing aspect ratio between the remaining two axes (α).

functions for filamentarity and planarity are plotted for a spheroid, by integrating the analytical forms of the Minkowski functionals for a spheroid while varying the aspect ratio between one axis and the two others. In addition to the spheroid reference lines the deformation of a spheroid through a general ellipsoid while keeping the volume and major axis length constant is provided, including the aspect ratio of the two remaining axis as α (it can for example be seen that a prolate spheroid with $\lambda = 2$ becomes an oblate spheroid with $\lambda = 1/4$).

Object tilt and orientation

As the Minkowski functionals (detailed in the previous section) only provide measures of scale, but not orientation, of individual objects, we introduce a means of calculating the x - y -plane orientation (ϕ , measured from the x -axis) and tilt (θ , measured from the z -axis) of an individual object (see Figure 5). The characteristic tilt and orientation for an individual coherent structure is calculated by first forming a *centerline* through the centroids of vertically adjacent slices of a given structure, and then computing the area-weighted angular average of z -tilt and x - y -orientation along this centreline (see appendix C for details).

4 | RESULTS

In this section we analyse the sheared and non-sheared simulations with the methods detailed above. The analysis first focuses on extracting characteristic length-scales of different fields in the boundary layer as a whole without attempting to identify individual coherent structures. Later the boundary layer air likely feeding convective clouds is identified. And lastly, properties of *individual* coherent structures are studied with the aim of revealing the properties of coherent structures that dominate the vertical moisture flux.

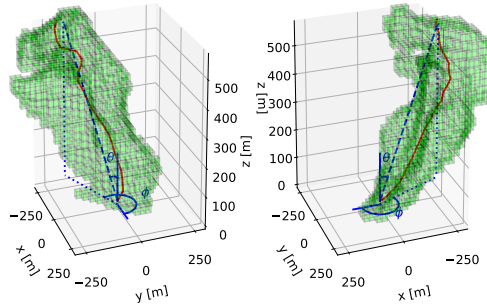


FIGURE 5 Voxel-rendering of single coherent structure from sheared simulation from two viewing angles, with object orientation angles θ (tilt from z -axis) and ϕ (xy -orientation from x -axis) and centerline (red) indicated.

4.1 | Vertical profiles of characteristic horizontal scales

To study the vertical transport produced by coherent structures in the boundary layer we must first formulate how to define these structures. Unfortunately the different scalar fields that are connected with transport relevant to moist convection (vertical velocity, buoyancy, moisture and heat content) vary on very different length-scales and these scales change with height in the boundary layer. To demonstrate this variability Figure 6 and 7 show the 2nd cumulant of vertical velocity with itself ($c_{w,w}$, the auto-correlation) and the 2nd cumulant of vertical velocity and liquid water potential temperature ($c_{w,\theta}$) in horizontal plane mid boundary-layer ($z = 300$ m).

Considering first the auto-correlation of vertical velocity ($c_{w,w}$), we note that vertical velocity features are elongated with ambient shear and axisymmetric without shear, as expected. The coherence length-scale (slashed vertical line) is largest in the middle of the boundary layer where vertical velocity peaks before thermals are decelerated becoming negatively buoyant in the relatively warm and dry layer below cloud.

Considering instead $c_{w,\theta}$, there is narrow length-scale of positive correlation until $z \approx 200$ m embedded within a larger-scale negative correlation. The positive correlation is provided by buoyancy in turn induced by sensible surface heat fluxes. However given that RICO represents shallow convection over the ocean (making the Bowen ratio small), the buoyancy becomes dominated by water vapour, and above $z \approx 200$ m, the correlation with potential temperature becomes negative. This transition causes the correlation length-scale to increase with height until $z \approx 200$ m, above which the larger-scale negative correlation takes over. In simulations with ambient shear the correlation between vertical velocity and temperature is not only elongated in the direction of shear, but the correlation is asymmetric in the direction of shear. This means that potential temperature features are displaced in the downwind direction relative to the vertical velocity, suggesting that the similarity solutions that assume radially symmetric distributions of different scalar fields (i.e. all scalar fields are assumed to be a function of a single radius r), as most plume-based models do (e.g. Devenish et al., 2010), may not be valid in conditions where shear is present.

To examine the variation in correlation length-scale with height, the cumulant-based coherence calculation was carried out at every model level in the boundary layer. Fig. 8 shows the autocorrelation length-scale as a function of height for both the sheared and non-sheared simulations. In the discussion below, subscript S and NS will be used to denote properties extracted from the shear and non-sheared simulations respectively. Comparing first the characteristic length-scales across different fields the vertical velocity is consistently confined to narrower features, whereas moisture and sensible heat organise on larger scales. The characteristic length-scale of the radioactive tracer

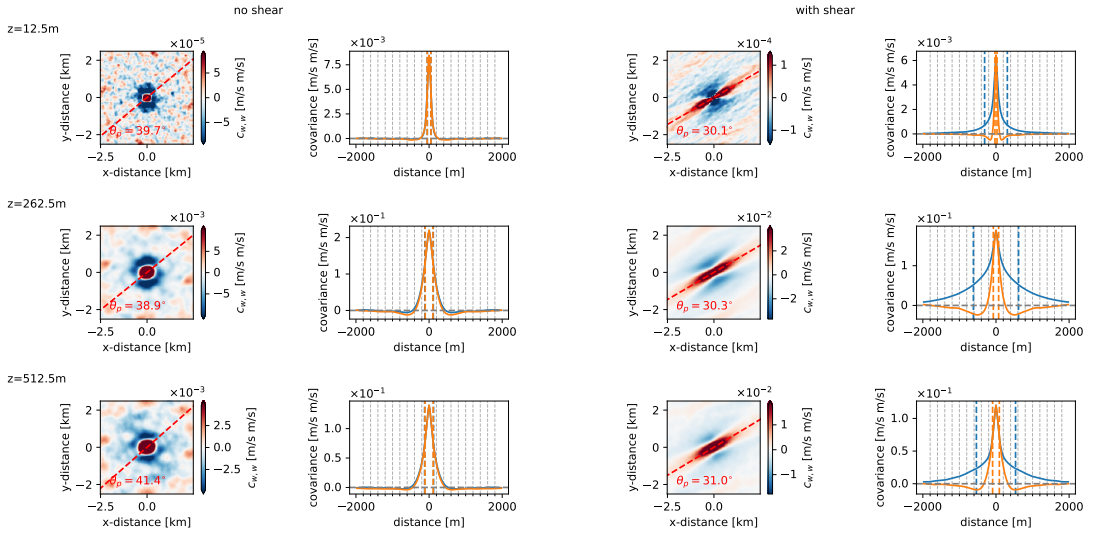


FIGURE 6 2nd cumulant of vertical velocity with vertical velocity at increasing heights in the boundary layer in simulations without shear (leftmost two columns) and with shear (rightmost two columns). At each height the cumulant (left, measuring coherence as a function of distance) is associated with the same cumulant sampled along the identified principle and perpendicular direction of coherence (right) with the calculated coherence length-scale indicated with slashed vertical lines. Note the magnitude of coherence changes with height.

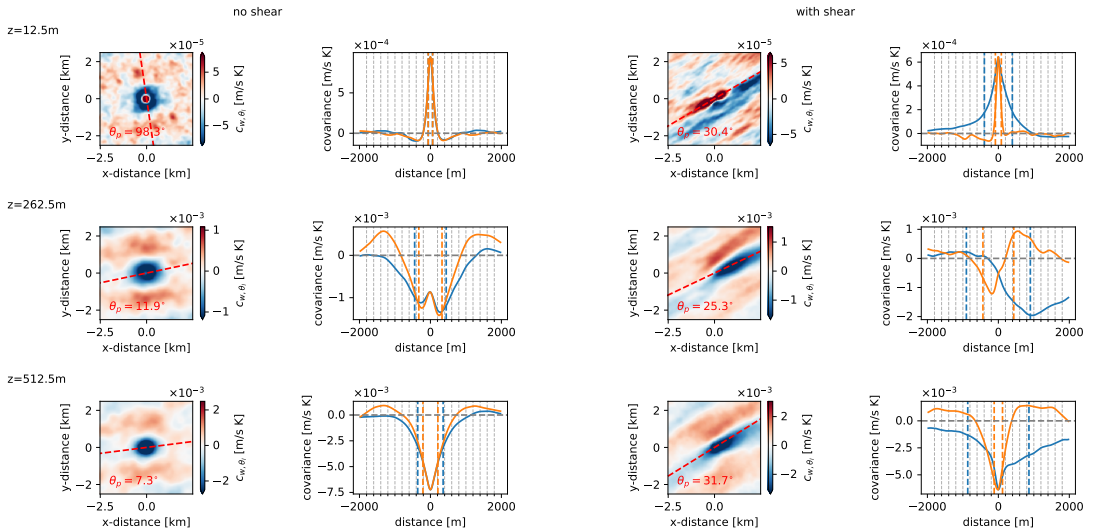


FIGURE 7 2nd cumulant of vertical velocity with liquid water potential temperature (panels as in Figure 6)

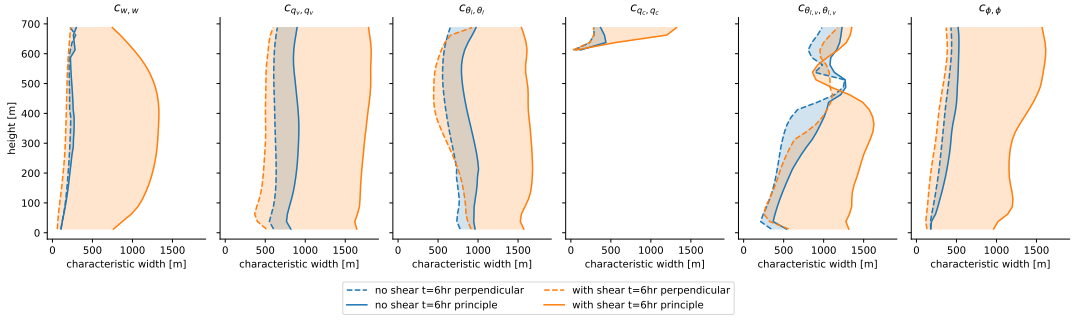


FIGURE 8 Horizontal coherence length-scales of vertical velocity (w), water vapour (q_v), liquid water potential temperature (θ_l), cloud water (q_c), virtual liquid water potential temperature ($\theta_{l,v}$) and the radiative passive tracer (ϕ), for simulations with shear (solid lines) and without shear (dashed lines).

field is generally larger than that for vertical velocity, possibly owing to the tracer concentration retaining high values in over-turning vortices of thermals within which the vertical velocity becomes negative.

In both simulations, with and without shear, the vertical velocity length-scale increases with height from the surface as thermals are accelerated by the buoyancy provided through surface fluxes, reaching a maximum scale of $L_{w,w}^P|_{NS} \approx 300$ m and $L_{w,w}^P|_S \approx 1300$ m at $z \approx 400$ m. Above this height, velocity scale stagnates (no shear) or decreases (with shear) with height, as the buoyancy of the rising coherent structures becomes negative and the structures begin decelerating through the CIN-layer. This effect of buoyancy on the correlation length-scale is more clearly seen when investigating the cross-correlations with vertical velocity (see below). Comparing the moisture and virtual liquid potential temperature (buoyancy) length-scales with the radioactive tracer, it is notable that although the buoyancy is water-vapour dominated, the length-scales of correlation of water vapour ($L_{q_v,q_v}^P|_{NS} \approx 600$ m and $L_{q_v,q_v}^P|_S \approx 500$ m at $z \approx 300$ m) are significantly larger than those of both the radioactive tracer ($L_{\phi,\phi}^P|_{NS} \approx 400$ m and $L_{\phi,\phi}^P|_S \approx 300$ m at $z \approx 300$ m) and than the buoyancy features ($L_{\theta_{l,v},\theta_{l,v}}^P|_{NS} \approx 500$ m and $L_{\theta_{l,v},\theta_{l,v}}^P|_S \approx 500$ m at $z \approx 300$ m). This means that larger-scale water vapour variability is producing buoyancy on a shorter length-scale, which in turn is accelerating boundary layer air on an even shorter length-scale. This is important for modelling, as the variability of the buoyancy scalar (here water vapour) cannot simply be used to infer the scale of coherent rising structures. Lastly, the maximum correlation length-scale of cloud water (a measure of cloud-size) is on the order of $L_{q_c,q_c}^P|_{NS} \approx 400$ m and $L_{q_c,q_c}^P|_S \approx 300$ m at $z \approx 650$ m (near cloud-base), showing most similarity to the radioactive tracer coherence length-scale at cloud-base.

The direction of longest correlation distance (see Fig. 9) is for all fields (including cloud water) oriented with the ambient wind-direction, which is also the principle direction of shear, throughout the boundary-layer and into cloud-base. In the absence of shear, some fields demonstrate some degree of turning with height, but examining multiple timesteps this was seen to be a transient feature, so that no preferential orientation can be discerned.

Applying the same analysis to the vertical fluxes of heat, moisture, buoyancy and radioactive tracer (Fig. 10) we see that these features are generally narrower than the scalar being transported, suggesting that the scale of vertical velocity is dominating the length-scales of vertical transport. All flux fields show clear elongation by ambient shear. The heights at which the correlation is negative is marked by minus-sign markers ("-") showing again the transitions for heat (at $z \approx 200$ m the heat flux changes sign) and buoyancy (at $z \approx 500$ m rising structures are no longer buoyant) where the correlation-length for both collapses. The moisture and radioactive tracer flux correlations (c_{w,q_v} and $c_{w,\phi}$) have near-monotonic increases in size with height until cloud-base is approached.

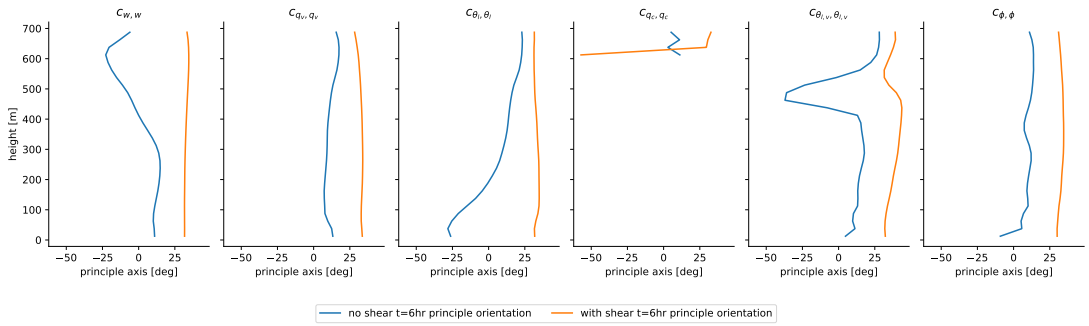


FIGURE 9 Direction of longest coherence as angle from x-axis (for the variables shown in Fig. 8). In the presence of ambient shear all fields are elongated in the direction of shear. In particular, note that cloud structures are elongated in the same direction as boundary layer structures.

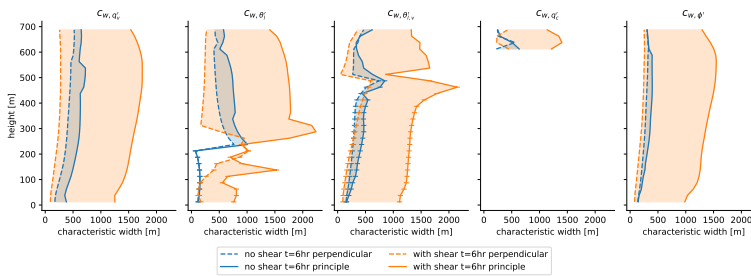


FIGURE 10 Horizontal coherence length-scales, in simulations with (orange lines) and without (blue lines) shear, of vertical velocity with water vapour, liquid water potential temperature, buoyancy (virtual liquid water potential temperature), cloud condensate and radioactive tracer effectively producing a coherence length-scale for the vertical flux for each scalar field. Heights at which anti-correlation occurs are marked with a minus-sign ("−").

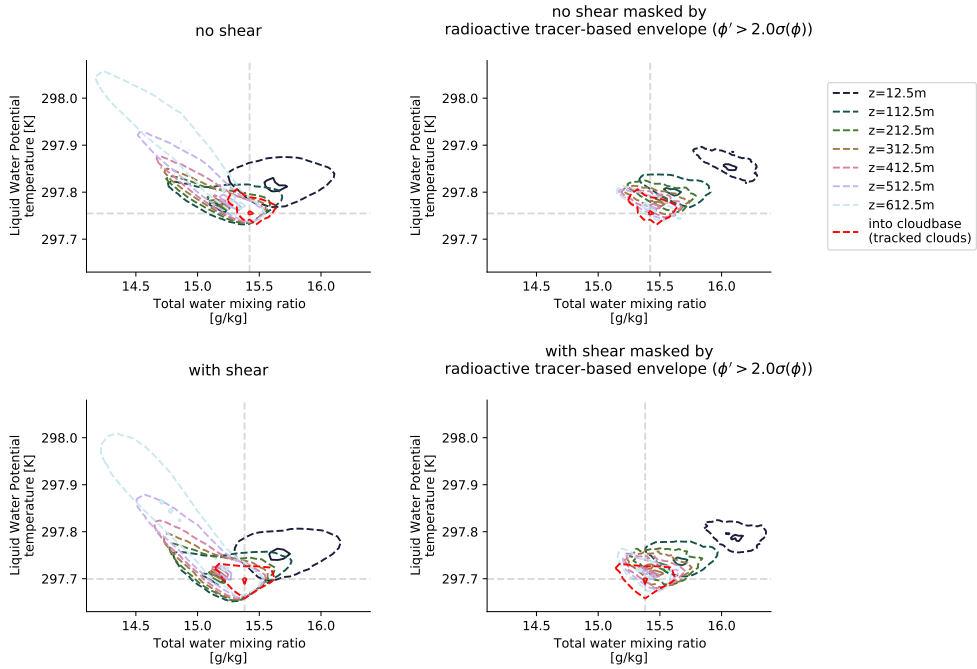


FIGURE 11 Joint distributions of total water vapour specific humidity and liquid potential temperature (same as potential temperature in the sub-saturated boundary layer below cloud) in horizontal cross-sections at increasing heights in the boundary layer together with properties of air entering through cloud-base of newly formed ($t_{age} < 3$ min) clouds in simulation with (bottom) and without (top) shear, both without (left) and with (right) the radioactive tracer mask applied. For each height and cloud-base properties the inner and outermost contours identify the regions which cumulatively contain the 10% and 90% highest point density, with the number of bins in θ_l and q_t scaling by the number of points, $N_{bins} = (N_x \times N_y)^{1/4}$. From a relatively moist and warm near-surface state the distribution first dries and cools into the bulk of the boundary layer, then warms and dries with height as air subsiding through the boundary layer top imparts a stronger influence.

4.2 | Cross-correlation of scalar fields

As shown above, different scalar fields show different length-scales of coherence and so we now turn to investigating the extent to which these fields are correlated, not in space but in the distributions of their scalar values. In Fig. 11 for the simulations with (right) and without shear (left) the joint distribution of water vapour and potential temperature through horizontal cross-sections at increasing heights are plotted. At each height a bivariate histogram was created, the bins ranked by number of points and contours drawn around the bins with 10% (inner contour, solid lines) and 90% (outer contour, stippled lines) cumulative point count. Constructed in this way the set of contours at each height identify the centre and width of the joint distribution for the scalar fields visualised (forming a 2D *box-and-whisker* plot). For reference, the boundary layer mean values for potential temperature and moisture are included. In addition to the distributions in horizontal cross-sections, the joint distribution for points immediately below (grid-spacing $\Delta z = 25$ m) cloud of newly-formed ($t_{age} < 3$ min) clouds (identified by cloud-tracking) is included.

The distributions have similar characteristics in the two simulations; near the surface the boundary layer is warm and moist relative to the boundary layer mean, through the super-adiabatic near-surface the distribution rapidly

becomes cooler and drier with height (until $z \approx 100$ m). With further increase in height the distribution is stretched to drier and warmer values as mixing with warm dry air subsiding through the boundary layer top has an increasing influence.

In both simulations, the distribution of air entering newly formed clouds (in red) coincides with the coldest and most humid part of the boundary layer joint distribution. The cloud-base distribution contains a larger range of moisture values in the simulation with shear, including drier parts of the bulk of the boundary layer distribution. This may be because ambient shear increases mixing into the rising coherent structures, carrying drier air in the regions with high vertical momentum or because the lower overall virtual potential temperature (buoyancy) of the boundary layer causes more air to be buoyant enough to rise to the level of condensation.

In addition, the distributions in the two simulations differ through a translation in potential temperature by approximately ≈ 0.1 K, which although small is on the order of the width of the distributions in both cases. This suggests that in the presence of shear the surface fluxes and subsiding air are less effective at heating the bulk of the boundary layer. This offset indicates that even in conditions where the prescribed surface fluxes are exactly the same, the dynamics of boundary layer transport can vary to a degree that alters the property of air that forms clouds, and so thresholds based solely on the thermodynamic fields (e.g. θ_l and q_l) are inadequate in identifying air that will form clouds.

It is clear from these joint distributions that if the aim is to characterise coherent structures which actually cause the formation of clouds, it is inadequate to simply construct a conditional sampling based on threshold values of the scalar fields causing transport. Instead a method that tracks air transported from the surface layer is required and to this end we in the next section employ a radioactively decaying tracer.

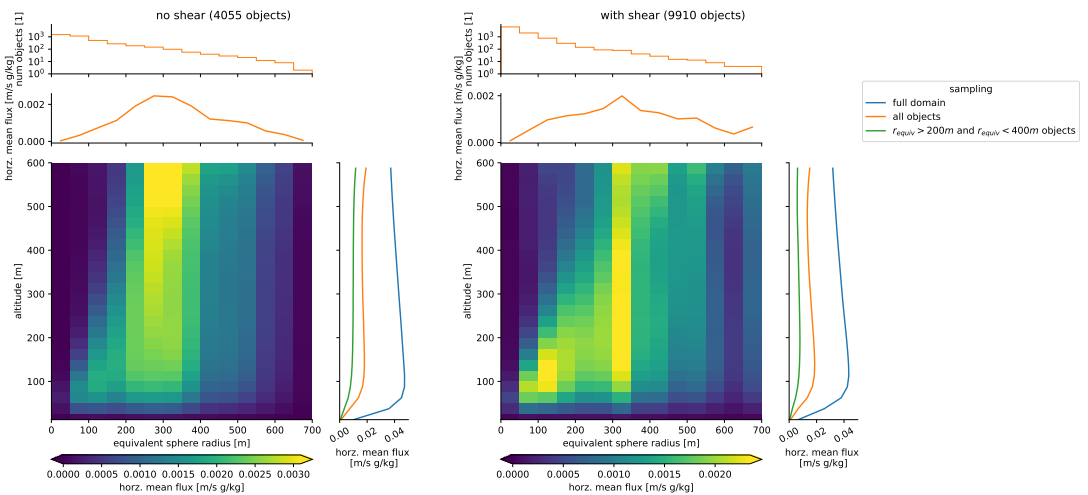


FIGURE 12 Vertical moisture flux decomposed by height and object equivalent radius, with size distribution of objects (top) and moisture flux profile (right). In the moisture flux profile the total domain mean (orange) is shown together with the moisture flux contributed by the selected objects (blue). The flux is carried, in aggregate, primarily by objects $r_{equiv} \approx 300$ m (the mean moisture-flux profile for objects in this range, $200 \text{ m} > r_{equiv} > 400 \text{ m}$, is given in green) and not by the order of magnitude more numerous smaller objects or relatively few larger objects.

4.3 | Identifying cloud-feeding coherent structures

We now turn to characterising the coherent structures that have the potential to trigger clouds. The joint distributions of the previous section are conditionally sampled (Fig. 11 right) by requiring that the concentration of decaying passive tracer is at least 2 standard deviations from the horizontal mean (see Sec. 3.2.1 for details).

Using this method for both the sheared and non-sheared simulations, distributions collapse down to align near-perfectly with that of air entering through cloud-base, indicating that the radioactive tracer is picking exactly the air that may trigger clouds. In addition, for both cases the means of the distributions appear to be near-linearly translated with height suggesting that these coherent cloud-triggering structures mix with the bulk of the boundary layer at a similar rate for both potential temperature and water vapour. Finally, the widths of the joint distributions appear nearly unchanged with height. All of these facts are encouraging for the prospect of parameterisation of the mixing into coherent updrafts in the boundary layer, by which the properties of cloud-triggering air may be predicted based on the surface fluxes (and other external forcing factors).

Although the radioactive tracer method identifies air with the same statistical properties as air that is triggering clouds, it is not guaranteed that every volume of this boundary layer air will actually trigger a cloud. Some structures may simply be too small to survive the journey to the condensation level without being completely mixed into the bulk boundary layer air. This can be addressed in further work by tracking boundary layer structures and identifying which ones actually trigger clouds (beyond the scope of this study). Here, we instead identify the structures that dominate the vertical moisture transport.

4.4 | Height and object-scale decomposition of vertical flux

Key to understanding the formation of clouds is to learn which coherent structures in the boundary layer collectively transport most of the vertical moisture flux. At either extreme one might believe that either the very few largest structures dominate, but equally the many orders of magnitude more numerous smallest structures could also collectively dominate the vertical flux. In Figure 12 the moisture flux is decomposed by object size (here equivalent spherical radius, $r_{equiv} = \sqrt[3]{3V/4\pi}$) and as a function of height, with the number of objects given along the top and total moisture flux profile along the right-hand side (total moisture flux in blue and flux carried by coherent structures denoted by orange markers). Note that an individual object of a given size will likely contribute to the flux at a number of different heights, and the figure simply shows at any given height which scale of objects contribute to the total moisture flux.

Examining first the horizontal mean flux, it is clear that approximately half of the vertical moisture flux is carried by the coherent structures which have been identified (the non-local transport), with a near-constant flux-profile with height, lending more credibility to the use of the radioactive tracer as a means to identify coherent structures in the boundary layer. The moisture flux is near-constant with height above $z \approx 100$ m, below which it appears to drop to zero near the surface. The moisture flux is in fact non-zero below this height, but is not carried by the resolved flow and is instead parameterised in the LES simulation as a sub-grid flux, providing the surface moisture source of the ocean surface.

By looking at the flux decomposition it can be seen that, above the surface-layer, objects of equivalent radius in the range $r_{equiv} \in [250 \text{ m}, 400 \text{ m}]$ dominate the moisture flux, carrying, in aggregate, $\approx 55\%$ and $\approx 42\%$ (in the simulations without and with shear respectively) of the vertical moisture flux between $z = 100$ m and $z = 500$ m. And so although there are only on the order of hundreds of objects of this size, they transport the majority of the vertical moisture flux.

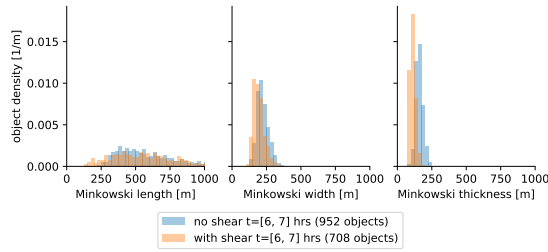


FIGURE 13 Distribution of Minkowski length, width and thickness for individual coherent structures identified in simulations with and without shear. Shear is seen to cause objects to become longer and thinner on average.

4.5 | Minkowski characteristics of coherent structures

Having identified the coherent structures with correct thermodynamic properties (for triggering clouds) and carrying the majority of the vertical moisture, we next calculate characteristic properties of each structure and attempt to quantify the difference in these structures with and without the presence of ambient shear. To do this we calculate a characteristic length, width and thickness for each object using the so-called Minkowski functionals (detailed in Sec. 3.2.2).

The distributions of these (Figure 13) show that, both with and without shear, the moisture flux transport is carried primarily by structures which are long and thin, and that these structures become longer and thinner in the presence of shear. In both simulations some objects have a Minkowski length longer than the depth of the boundary layer depth because they extend in both the horizontal and vertical direction.

This shift in the distribution can be succinctly captured by computing the filamentarity and planarity (measuring how *pencil-like* or *disc-like* object each is) as seen in Figure 14, showing that ambient shear causes the coherent structures to become more elongated and planar at the same time, which can be seen by a $\approx 30\%$ increase in filamentarity ($F_{NS} \approx 0.45$ and $F_S \approx 0.6$) and $\approx 60\%$ increase in planarity ($P_{NS} \approx 0.15$ and $P_S = 0.25$). As a reference (in black), the filamentarity and planarity of an ellipsoid with varying elongation (parameterised as the aspect ratio between one axis and the remaining two) the coherent structures can be seen to move from being more cylindrical to sheet-like in shape.

4.6 | Object orientation

In addition to knowing the characteristic length-scales and shape of individual coherent structures it is instructive to determine the tilt and orientation of each object to be able to formulate an integral model to represent transport by coherent structures. In Figure 15, the tilt and orientation angles for all objects present at $t = 6$ h in both the simulation with and without shear are plotted. This shows the presence of ambient shear ($\approx 2 \text{ m s}^{-1}$ change in wind-speed over the sub-cloud layer) caused the mean tilt of individual objects to change from $\theta_{no, shear} \approx 10^\circ$ (near-vertical, given the near symmetrical angular spread in orientation angle) to $\theta_{shear} \approx 30^\circ$ and changed the structures from having no preferential horizontal orientation, to being oriented with direction of wind shear ($\phi_{shear} \approx 210^\circ$). The principal orientation direction in the presence of shear was found to agree with the direction of coherence elongation found using cumulants. This suggests that individual coherent structures tilt in the same direction that the structures spatially align along (as the cumulant-based technique cannot separate elongation of individual structures from spatial organisation of individual structures).

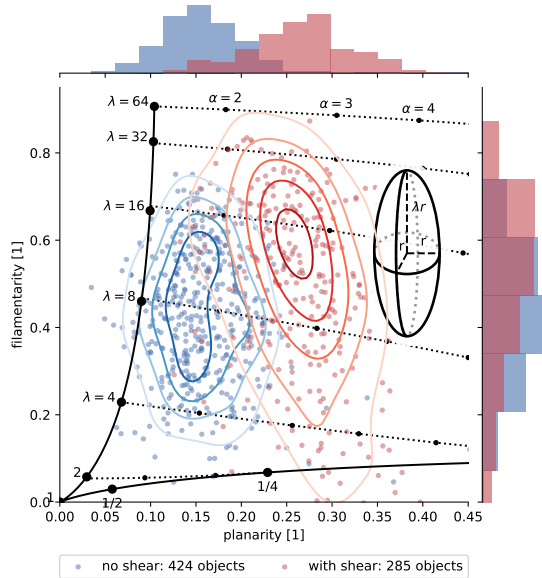


FIGURE 14 Filamentarity vs planarity for coherent structures dominating the vertical moisture flux ($r_{equiv} > 200$ m and $r_{equiv} < 400$ m) in simulations with (red) and without shear (blue), together with spheroid reference (solid black) with independent axis parameterised by λ and deformation of a spheroid through a general ellipsoid with fixed major axis and varying aspect between the remaining two axes (α).

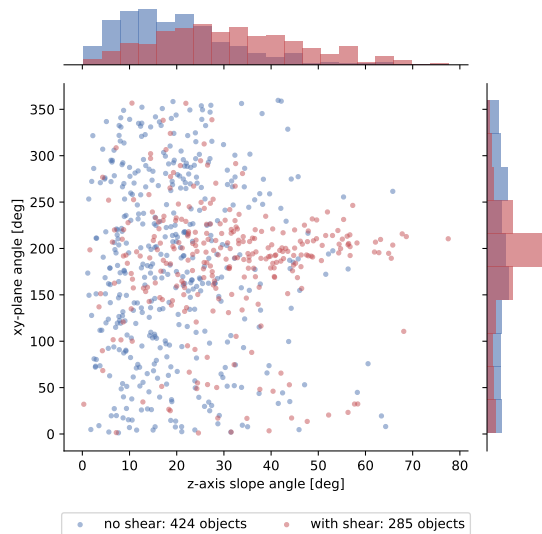


FIGURE 15 xy-orientation angle (ϕ) against z-axis slope angle (θ) for objects dominating the vertical moisture flux ($r_{equiv} > 200$ m and $r_{equiv} < 400$ m) present at $t = 6$ h in simulations with (red) and without shear (blue), together with distributions in each along plot margins

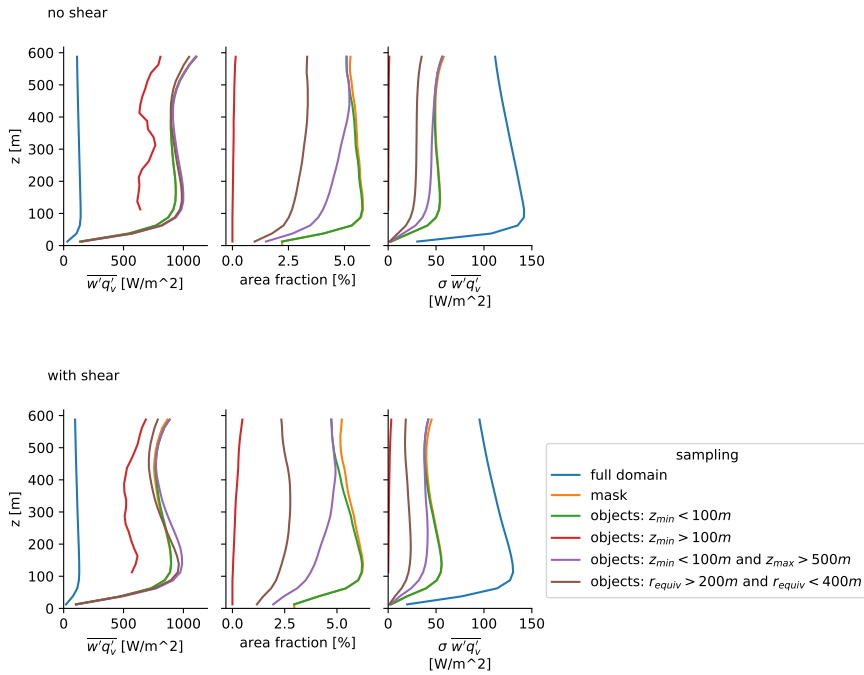


FIGURE 16 Vertical profiles of mean moisture flux, area fraction and mean total moisture flux conditionally sampled by passive tracer mask, objects attached and detached from surface and entire domain for simulation with (bottom) and without (top) shear at $t = 6$ h.

4.7 | Plume vs thermal - vertical extent vs height

Having decomposed the coherent transport in the boundary layer into contributions by individual coherent structures the question of whether these structures are more thermal- or plume-like may be investigated by considering the vertical extent of each structure. As plumes must be continuously fed from below, these objects must extend the full length from the surface layer to the cloud-base to constitute plume-like objects.

Figure 16 explores this (for the simulations with and without shear respectively) by plotting the in-object mean moisture flux profile, area-fraction and contribution to the domain mean moisture flux. Together with the domain-wide and passive tracer mask mean, the mean moisture flux contributed by objects attached ($z_{min} < 100$ m) and detached ($z_{min} > 100$ m) from the surface are plotted, as well as the mean moisture flux for objects which extend the full height of the boundary layer ($z_{min} < 100$ m and $z_{max} > 500$ m). Comparing first the profiles for objects attached and detached from the surface it is clear that very little moisture flux is actually carried by thermal-like coherent structures detached from the surface. Further, the plume-like coherent structures that are attached to the surface *and* extend to cloud base carry $> 80\%$ of the moisture flux carried by coherent structures, with only a small fraction carried by shorter structures below the middle of the boundary layer. The contribution by different coherent structures to the total moisture flux can largely be explained by change in fractional area covered by different groups of coherent structures, whereas the change in mean in-object moisture flux is nearly unchanged between the different groups of structures.

In both simulations the horizontal area-fraction covered by all identified coherent structures decreases with height through the boundary layer (from $\sigma|_S(z \approx 100 \text{ m}) \approx 6\%$ to $\sigma|_S(z \approx 600 \text{ m}) \approx 5\%$) as does the mean in-structure moisture

flux $\overline{w'q'_v}|_S(z \approx 100 \text{ m}) \approx 1000 \text{ W}^2 \text{ m}^{-1}$ to $\overline{w'q'_v}|_S(z \approx 600 \text{ m}) \approx 800 \text{ W m}^{-2}$), although for the case without shear these decreases are less pronounced. These decreases together lead to a decrease in the contribution to domain-mean moisture flux contribution from coherent structures with height. The small area-fraction of coherent structures here (as compared to work by Efstathiou et al., 2020) is likely due to using a standard deviation scaling ($n = 2$ here) in line with work by Chinita et al. (2018).

When considering only the the plume-like coherent structures the area-fraction covered increases with height (from $\sigma|_S(z \approx 100 \text{ m}) \approx 3\%$ to $\sigma|_S(z \approx 600 \text{ m}) \approx 5\%$) as these structures entrain boundary layer air, but this is compensated by a decrease with height in mean in-structure moisture flux (as the coherent structures dry through mixing with the boundary layer air) to give a near-constant moisture flux profile with height.

For comparison, the mean moisture flux for the flux-dominating coherent structures ($r_{equiv} > 200 \text{ m}$ and $r_{equiv} < 400 \text{ m}$) is given, showing the same near-constant profile and accounting for $\approx 2/3$ of the flux carried by plume-like coherent structures.

5 | DISCUSSION

The pre-cloud coherent boundary layer structures (identified using a decaying passive tracer) which in aggregate carry a large fraction of the vertical moisture flux ($\approx 55\%$ and $\approx 42\%$ of the moisture flux between $z = 100 \text{ m}$ and $z = 500 \text{ m}$ in the simulations without and with shear respectively), have volumes equivalent to a spherical radius of $200 \text{ m} < r_{equiv} < 400 \text{ m}$. In addition, the structures that dominate the vertical moisture flux extend from the surface to the cloud layer (in both simulations with and without shear), suggesting they are more plume-like than thermal-like in morphology. The presence of ambient shear is seen to tilt the coherent objects from being nearly vertical to being oriented at 30° from the z-axis in the direction of the ambient wind. The presence of shear also causes the structures to become elongated and more planar, by $\approx 30\%$ and $\approx 60\%$ respectively. These findings suggest that models representing non-local transport by coherent boundary layer structures, should chose the plume model as the fundamental starting point and may find that boundary layer transport can be adequately represented by a plume with characteristic width on the scale of the boundary layer depth. The effect of ambient shear appears to be to organise vertical transport into coherent structures which are elongated (which would increase entrainment by increasing the surface area) and stretched planar, and at the same time organised into linear features (which may decrease entrainment by limiting the dry air reaching individual plumes). Understanding the competing effects of shear in future work and allowing for non-radially symmetric plumes is key to allowing for better representation in parameterisations.

The moisture flux profiles, when considering all coherent structures identified, decrease with height in both simulations, but to a larger extent in the simulation with shear ($\approx 100 \text{ W m}^{-2}$ vs $\approx 250 \text{ W m}^{-2}$), which arises by a marked decrease in area fraction in both simulations and in-object mean flux in the case with ambient shear. However, when only considering the objects that dominate the moisture flux transport ($200 \text{ m} < r_{equiv} < 400 \text{ m}$) their area-fraction increases with height, compensating for the in-structure drop in mean moisture-flux, resulting in a almost identical moisture flux profile for the two simulations when only considering these flux-dominating structures. This suggests that although the spatial organisation of coherent boundary layer structures is different in the simulations with and without shear, and the in-structure flux and area fraction is affected by shear, the total flux contribution by coherent structures appears relatively unchanged under the introduction of shear.

The two methods presented here, the first focusing on bulk-measures of coherence in the boundary layer (using cumulants) and the second on identifying and quantifying properties of individual coherent structures (using Minkowski functionals, tilt/orientation calculation and flux decomposition), have complementary strengths.

The principal difference between the two approaches is that the cumulant-based method produces a length-scale estimate through considering the spatial coherence throughout the fluid, whereas identifying and characterising individual objects gives an estimate of scale for individual coherent structures. Two individual objects in close proximity will increase the cumulant length-scale estimate, meaning that the cumulant length-scale conflates the object size and object organisation (specifically the inter-object distance). In addition, in cases where there are multiple populations of coherent structures, the cumulant method will conflate these into one integrated measure, and the relevant details of each separate population may be lost. In particular, in the upper part of the boundary layer which is characterised by ascending buoyant thermals and descending entrainment flows, the cumulant analysis will not necessarily give a "clean" description of either of these.

Another aspect by which the two approaches differ is how the cumulant method estimates length-scales in the horizontal plane (the method requires translational symmetry to study coherence as a function of displacement and so cannot be applied vertically without picking a reference height), whereas the length-scales of individual objects are not constrained in the orientation in which these length-scales are calculated. This firstly means that the two measures of length cannot be directly compared, as the Minkowski length-scales are not measured in the horizontal plane and necessitate the calculation of object orientation to interpret the length-scales calculated.

Finally, the cumulant-based method *does* produce a bulk estimate of the orientation of coherent structures (or the direction of their relative positioning), but in the horizontal plane and so this estimate lacks information about the tilt of individual coherent structures. The Minkowski functionals do not provide measures of direction, only scale, another reason why the use of Minkowski functionals was supplemented by a separate method to estimate the tilt and orientation of individual objects.

6 | CONCLUSIONS AND FURTHER WORK

This paper has demonstrated two methods by which to measure cloud-feeding coherent structures in the atmospheric boundary layer. The first method quantifies the horizontal orientation and length-scale of coherence between any two scalar fields, and through this makes it possible to measure the coherence in the boundary layer as a whole. The second method identifies cloud-feeding coherent structures using a decaying passive tracer and is able to quantify length-scales and orientation (both vertical and horizontal) for each of these objects, allowing for a more instructive decomposition where the non-local transport by individual coherent structures can be studied.

We have demonstrated the use of cumulants to measure characteristic length-scales for different scalar fields and fluxes of these fields in the bulk of the boundary layer. This showed that vertical velocity features are significantly narrower (≈ 500 m) than the moisture and potential temperature fields (≈ 1000 m). This method is also able to quantify the elongation of these coherent structures and calculate the elongation direction, showing how the presence of ambient wind shear causes elongation of the vertical velocity and a less-pronounced change to the heat and moisture fields.

We additionally demonstrated how a surface-released radioactive tracer may be used to identify air with the same statistical properties as air entering through cloud-base. This allowed for the development of a method to identify individual cloud-feeding coherent structures, which were then characterised using Minkowski functionals (producing a characteristic length, width and thickness for each object) and a technique for calculating an object's tilt and horizontal orientation. With these methods it was shown that the coherent structures which dominate the vertical moisture flux are plume-like in nature (being attached to the surface and reaching the cloud-layer), and that the presence of ambient shear causes significant elongation of these structures while causing them to tilt and orient in the direction of ambient

shear. These findings cannot be made through a bulk-estimate of length-scale of coherence, as was done in previous work, but requires identifying and measuring individual coherent structures.

These findings suggest that when formulating models to represent transport by pre-cloud coherent boundary layers structures, the most appropriate model may be a plume, at least for the kinds of boundary layer simulated here. In the presence of shear the elongation and tilting (likely increasing the entrainment of dry air) of these structures should be represented in parameterisations. Further study can explore the generality of this conclusion to other boundary layer configurations, e.g. land-based, heterogeneously forced, deep convective etc. The software implementation of the techniques presented here are available in Denby and Liberzon (2020).

This work used the ARCHER UK National Supercomputing Service (www.archer.ac.uk) and was funded through the NERC/Met Office Joint Programme "Understanding and Representing Atmospheric Convection across Scales (ParaCon)", grant NE/N013840/1.

A | TIME-SCALE OF CONVECTIVE OVERTURNING IN BOUNDARY LAYER

Using the sub-cloud characteristic velocity scale w_* (as in Holtslag and Nieuwstadt, 1986, but corrected for the contribution to buoyancy from water vapour) and the boundary layer depth z_{BL} we can calculate a sub-cloud convective overturning time-scale τ_{BL} as

$$\tau_{BL} = \frac{z_{BL}}{w_*} \quad (13)$$

The sub-cloud convective velocity scale is given as

$$w_* = \left(\overline{w'b'} \Big|_0 \right)^{1/3}, \quad (14)$$

with buoyancy flux

$$\overline{w'b'} \Big|_0 = \frac{g}{T_{v,0}} \overline{w'\theta'_v} \Big|_0, \quad (15)$$

and virtual potential temperature flux (approximately) given by (de Roode et al., 2004)

$$\overline{w'\theta'_v} \Big|_0 = \overline{w'\theta'} \Big|_0 + \frac{R_v}{R_d} \bar{\theta}_0 \overline{w'q'} \Big|_0, \quad (16)$$

where z_{BL} is the boundary-layer depth, g the gravitational acceleration and $|_0$ denotes surface values. With surface fluxes for sensible $\overline{w'\theta'} \Big|_0 = \frac{F_s}{\rho_0 c_{p,d}}$ and latent heat $\bar{\theta}_0 \overline{w'q'} \Big|_0 = \frac{F_v}{\rho_0 L_v}$, surface moisture $q_{v,0} = 15 \text{ g kg}^{-1}$, surface temperature $T_0 = 300 \text{ K}$ and diagnosed boundary-layer depth $z_{BL} = 650 \text{ m}$ (here taken as the cloud-base height) the convective overturning time-scale becomes $\tau_{BL} = 16 \text{ min}$. The constants used above are those for density of dry air $\rho_0 = 1.2 \text{ kg m}^{-3}$, latent heat of vaporisation $L_v = 2.5 \times 10^6 \text{ J kg}^{-1}$, specific heat capacity of dry air $c_{p,d} = 1005 \text{ J kg}^{-1} \text{ K}^{-1}$, gas constants for dry air $R_d = 287287 \text{ J kg}^{-1} \text{ K}^{-1}$ and water vapour $R_v = 461 \text{ J kg}^{-1} \text{ K}^{-1}$.

B | CROFTON'S FORMULA FOR DISCRETE INTEGRALS

Numerically evaluating the integrals of the Minkowski functionals in 3D (equations 7 to 10) is non-trivial on discrete 3D masks as these structures are necessarily blocky and so constructing, for example, the surface normal at a corner is poorly defined.

Instead of approximating the surface normals, the Minkowski integrals can be approximated discretely using Crofton's formula. This amounts to counting the number of vertices (N_0), edges (N_1), faces (N_2) and cells (N_3) on both the interior and exterior of a given object mask. With these the Minkowski functionals in 3D are given as

$$V_0 = N_3, V_1 = 2 \frac{N_2 - 3N_3}{9\Delta x}, V_2 = 2 \frac{N_1 - 2N_2 + 3N_3}{9\Delta x^2},$$

$$V_3 = \frac{N_0 - N_1 + N_2 - N_3}{\Delta x^3}.$$

It can be shown for shapes where analytical forms for the Minkowski functionals exist that these approximate definitions converge to the true values when $\Delta x \rightarrow \infty$. **Note** that the above approximations assume the underlying grid to have isotropic grid spacing ($\Delta x = \Delta y = \Delta z$).

C | CALCULATION OF SLOPE AND ORIENTATION OF INDIVIDUAL OBJECTS

The xy -orientation angle (ϕ measured from the x -axis) and tilt angle θ (measured from the z -axis) are calculated from characteristic slope scales $\overline{\Delta x}$, $\overline{\Delta y}$, $\overline{\Delta z}$:

$$\phi = \arctan 2(\overline{\Delta y}, \overline{\Delta x}), \theta = \arctan 2(\overline{\Delta l_{xy}}, \overline{\Delta z}), \Delta l_{xy} = \sqrt{\overline{\Delta x}^2 + \overline{\Delta y}^2},$$

which are evaluated as area-weighted changes in the centroid position

$$\overline{\Delta x} = \frac{\Delta z}{V} \sum_k A(z_k) \frac{x^c(z_{k+1}) - x^c(z_{k-1})}{2}, \overline{\Delta y} = \frac{\Delta z}{V} \sum_k A(z_k) \frac{y^c(z_{k+1}) - y^c(z_{k-1})}{2}, \overline{\Delta z} = \frac{\Delta z}{V} \sum_k A(z_k) \frac{z^c(z_{k+1}) - z^c(z_{k-1})}{2},$$

where $x_c(k)$, $y_c(k)$ and $A(k)$ are the centroid x and y position, and area at height-index k respectively, and V the volume, given by

$$A(z_k) = \sum_{i,j} m(x_i, y_j, z_k) \Delta x \Delta y, V = \sum_{i,j,k} m(x_i, y_j, z_k) \Delta x \Delta y \Delta z$$

$$x^c(z_k) = \frac{\sum_{i,j} x_i m(x_i, y_j, z_k)}{\sum_{i,j} m(x_i, y_j, z_k)}, y^c(z_k) = \frac{\sum_{i,j} y_j m(x_i, y_j, z_k)}{\sum_{i,j} m(x_i, y_j, z_k)}$$

for an individual object defined by the mask m and grid-spacing Δx , Δy , Δz .

REFERENCES

- Ait-Chaalal, F., Schneider, T., Meyer, B. and Marston, J. B. (2016) Cumulant expansions for atmospheric flows. *New Journal of Physics*, **18**.
- Berg, L. K. and Stull, R. B. (2004) Parameterization of joint frequency distributions of potential temperature and water vapor mixing ratio in the daytime convective boundary layer. *Journal of the Atmospheric Sciences*, **61**, 813–828.
- Bony, S., Stevens, B., Ament, F., Bigorre, S., Chazette, P., Crewell, S., Delanoë, J., Emanuel, K., Farrell, D., Flamant, C., Gross, S., Hirsch, L., Karstensen, J., Mayer, B., Nuijens, L., Ruppert, J. H., Sandu, I., Siebesma, P., Speich, S., Szczap, F., Totems, J., Vogel, R., Wendisch, M., Wirth, M., Siebesma, P., Crewell, S., Wendisch, M., Totems, J., Delanoë, J., Sandu, I., Nuijens, L., Speich, S., Bigorre, S., Chazette, P., Stevens, B., Gross, S., Ament, F., Farrell, D., Bony, S., Hirsch, L., Mayer, B., Ruppert, J. H., Flamant, C., Karstensen, J., Wirth, M., Emanuel, K. and Szczap, F. (2017) EUREC4A: A Field Campaign to Elucidate the Couplings Between Clouds, Convection and Circulation. *Surveys in Geophysics*, **38**, 1529–1568. URL: <http://link.springer.com/10.1007/s10712-017-9428-0>.
- Brient, F., Couvreur, F., Villefranque, N., Rio, C. and Honnert, R. (2019) Object-Oriented Identification of Coherent Structures in Large Eddy Simulations: Importance of Downdrafts in Stratocumulus. *Geophysical Research Letters*, **46**, 2854–2864.
- Brown, A. R. and Grant, A. L. (1997) Non-local mixing of momentum in the convective boundary layer. *Boundary-Layer Meteorology*, **84**, 1–22.
- Chinita, M. J., Matheou, G. and Teixeira, J. (2018) A joint probability density-based decomposition of turbulence in the atmospheric boundary layer. *Monthly Weather Review*, **146**, 503–523.
- Couvreur, F., Hourdin, F. and Rio, C. (2010) Resolved Versus Parametrized Boundary-Layer Plumes. Part I: A Parametrization-Oriented Conditional Sampling in Large-Eddy Simulations. *Boundary-Layer Meteorology*, **134**, 441–458. URL: <http://link.springer.com/10.1007/s10546-009-9456-5>.
- Dawe, J. T. and Austin, P. H. (2012) Statistical analysis of an les shallow cumulus cloud ensemble using a cloud tracking algorithm. *Atmospheric Chemistry and Physics*, **12**, 1101–1119.
- Deardorff, J. W. (1966) The Counter-Gradient Heat Flux in the Lower Atmosphere and in the Laboratory. *Journal of the Atmospheric Sciences*, **23**, 503–506. URL: <http://repositorio.unan.edu.ni/2986/1/5624.pdf>.
- Denby, L. and Liberzon, A. (2020) GENESIS toolkit for analysing atmospheric coherent structures. URL: <https://zenodo.org/record/3956423>.
- Devenish, B. J., Rooney, G. G., Webster, H. N. and Thomson, D. J. (2010) The entrainment rate for buoyant plumes in a crossflow. *Boundary-Layer Meteorology*, **134**, 411–439.
- Efstathiou, G. A., Thuburn, J. and Beare, R. J. (2020) Diagnosing Coherent Structures in the Convective Boundary Layer by Optimizing Their Vertical Turbulent Scalar Transfer. *Boundary-Layer Meteorology*, **174**, 119–144. URL: <https://doi.org/10.1007/s10546-019-00480-1>.
- Etling, D. and Brown, R. A. (1993) Roll vortices in the planetary boundary layer: A review. *Boundary-Layer Meteorology*, **65**, 215–248.
- Grant, A. L. M. and Brown, A. R. (1999) A similarity hypothesis for shallow-cumulus transports. *Quarterly Journal of the Royal Meteorological Society*, **125**, 1913–1936. URL: <http://doi.wiley.com/10.1002/qj.49712555802>.
- Heus, T. and Seifert, a. (2013) Automated tracking of shallow cumulus clouds in large domain, long duration large eddy simulations. *Geoscientific Model Development*, **6**, 1261–1273.
- Holtslag, A. A. and Nieuwstadt, F. T. (1986) Scaling the atmospheric boundary layer. *Boundary-Layer Meteorology*, **36**, 201–209.

- Holtstag, A. A. M. and Moeng, C.-H. (1991) Eddy Diffusivity and Countergradient Transport in the Convective Atmospheric Boundary Layer. *Journal of the Atmospheric Sciences*, **48**, 1690–1698. URL: <https://journals.ametsoc.org/jas/article/48/14/1690/22553/Eddy-Diffusivity-and-Countergradient-Transport-in>.
- Jonker, H. J. J., Duynkerke, P. G. and Cuijpers, J. W. M. (1999) Mesoscale Fluctuations in Scalars Generated by Boundary Layer Convection. *Journal of the Atmospheric Sciences*, **56**, 801–808. URL: <http://journals.ametsoc.org/doi/abs/10.1175/1520-0469%281999%29056%3c0801%3AMFISGB%3E2.0.CO%3B2>.
- Khanna, S. and Brasseur, J. G. (1998) Three-dimensional buoyancy- and shear-induced local structure of the atmospheric boundary layer. *Journal of the Atmospheric Sciences*, **55**, 710–743.
- Lauritzen, S. L. (2007) Thiele: Pioneer in Statistics. URL: <http://www.oxfordscholarship.com/oso/public/content/math/9780198509721/toc.html>.
- Lenschow, D. H. and Sun, J. (2007) The spectral composition of fluxes and variances over land and sea out to the mesoscale. *Boundary-Layer Meteorology*, **125**, 63–84.
- Lohou, F., Druilhet, A., Campistron, B., Redelspergers, J. L. and Saïd, F. (2000) Numerical study of the impact of coherent structures on vertical transfers in the atmospheric boundary layer. *Boundary-Layer Meteorology*, **97**, 361–383.
- Mecke, K. R. (2000) Additivity, Convexity, and Beyond: Applications of Minkowski Functionals in Statistical Physics. In *Statistical Physics and Spatial Statistics*, 111–184. Berlin, Heidelberg: Springer Berlin Heidelberg. URL: http://link.springer.com/10.1007/3-540-45043-2_6.
- Miao, Q., Geerts, B. and LeMone, M. (2006) Vertical velocity and buoyancy characteristics of coherent echo plumes in the convective boundary layer, detected by a profiling airborne radar. *Journal of Applied Meteorology and Climatology*, **45**, 838–855.
- Minkowski, H. (1903) Volumen und Oberfläche. *Mathematische Annalen*, **57**, 447–495. URL: http://link.springer.com/10.1007/978-3-322-90190-3_7http://link.springer.com/10.1007/BF01445180.
- Nicholls, S. and Lemone, M. A. (1980) The fair weather boundary layer in GATE: the relationship of subcloud fluxes and structure to the distribution and enhancement of cumulus clouds.
- Park, S. B., Böing, S. and Gentine, P. (2018) Role of surface friction on shallow nonprecipitating convection. *Journal of the Atmospheric Sciences*, **75**, 163–178.
- Park, S. B., Gentine, P., Schneider, K. and Farge, M. (2016) Coherent structures in the boundary and cloud layers: Role of updrafts, subsiding shells, and environmental subsidence. *Journal of the Atmospheric Sciences*, **73**, 1789–1814.
- Poelaert, D., Schniewind, J. and Janssens, F. (2011) Surface Area and Curvature of the general Ellipsoid. 1–13. URL: <http://arxiv.org/abs/1104.5145>.
- Rauber, R. M., Ochs, H. T., Di Girolamo, L., Göke, S., Snodgrass, E., Stevens, B., Knight, C., Jensen, J. B., Lenschow, D. H., Rilling, R. A., Rogers, D. C., Stith, J. L., Albrecht, B. a., Zuidema, P., Blyth, a. M., Fairall, C. W., Brewer, W. A., Tucker, S., Lasher-Trapp, S. G., Mayol-Bracero, O. L., Vali, G., Geerts, B., Anderson, J. R., Baker, B. A., Lawson, R. P., Bandy, A. R., Thornton, D. C., Burnet, E., Brenguier, J.-L., Gomes, L., Brown, P. R. A., Chuang, P., Cotton, W. R., Gerber, H., Heikes, B. G., Hudson, J. G., Kollias, P., Krueger, S. K., Nuijens, L., O’Sullivan, D. W., Siebesma, A. P. and Twohy, C. H. (2007) Rain in Shallow Cumulus Over the Ocean: The RICO Campaign. *Bulletin of the American Meteorological Society*, **88**, 1912–1928. URL: <http://journals.ametsoc.org/doi/abs/10.1175/BAMS-88-12-1912>.
- de Roode, S. R., Duynkerke, P. G. and Jonker, H. J. (2004) Large-eddy simulation: How large is large enough? *Journal of the Atmospheric Sciences*, **61**, 403–421.
- Sahni, V., Sathyaprakash, B. S. and Shandarin, S. F. (1998) Shapefinders: A New Shape Diagnostic for Large-Scale Structure. *The Astrophysical Journal*, **495**, L5–L8.

- Salesky, S. T., Chamecki, M. and Bou-Zeid, E. (2017) On the Nature of the Transition Between Roll and Cellular Organization in the Convective Boundary Layer. *Boundary-Layer Meteorology*, **163**, 41–68.
- Schmalzing, J. and Buchert, T. (1997) Beyond Genus Statistics: A Unifying Approach to the Morphology of Cosmic Structure. *The Astrophysical Journal*, **482**, L1–L4.
- Schmalzing, J., Buchert, T., Melott, A. L., Sahni, V., Sathyaprakash, B. S. and Shandarin, S. F. (1999) Disentangling the Cosmic Web. I. Morphology of Isodensity Contours. *The Astrophysical Journal*, **526**, 568–578.
- Schmidt, H. and Schumann, U. (1989) Coherent structure of the convective boundary layer derived from large-eddy simulations. *Journal of Fluid Mechanics*, **200**, 511–562.
- Schumann, U. and Moeng, C.-H. (1991) Plume Fluxes in Clear and Cloudy Convective Boundary Layers. *Journal of the Atmospheric Sciences*, **48**, 1746–1757. URL: <https://journals.ametsoc.org/jas/article/48/15/1746/22406/Plume-Fluxes-in-Clear-and-Cloudy-Convective>.
- Seifert, A., Heus, T., Pincus, R. and Stevens, B. (2015) Large-eddy simulation of the transient and near-equilibrium behavior of precipitating shallow convection. *Journal of Advances in Modeling Earth Systems*, **7**, 1918–1937. URL: <http://doi.wiley.com/10.1002/2015MS000489>.
- Siebesma, A. P., Bretherton, C. S., Brown, A., Chlond, A., Cuxart, J., Duijkerke, P. G., Jiang, H., Khairoutdinov, M., Lewellen, D., Moeng, C.-H., Sanchez, E., Stevens, B. and Stevens, D. E. (2003) A Large Eddy Simulation Intercomparison Study of Shallow Cumulus Convection. *Journal of the Atmospheric Sciences*, **60**, 1201–1219. URL: <https://journals.ametsoc.org/jas/article/60/10/1201/103861/A-Large-Eddy-Simulation-Intercomparison-Study-of>.
- Siebesma, A. P., Soares, P. M. M. and Teixeira, J. (2007) A Combined Eddy-Diffusivity Mass-Flux Approach for the Convective Boundary Layer. *Journal of the Atmospheric Sciences*, **64**, 1230–1248.
- Stevens, B., Moeng, C.-H., Ackerman, A. S., Bretherton, C. S., Chlond, A., de Roode, S., Edwards, J., Golaz, J.-C., Jiang, H., Khairoutdinov, M., Kirkpatrick, M. P., Lewellen, D. C., Lock, A., Müller, F., Stevens, D. E., Whelan, E. and Zhu, P. (2005) Evaluation of Large-Eddy Simulations via Observations of Nocturnal Marine Stratocumulus. *Monthly Weather Review*, **133**, 1443–1462.
- Stevens, B. and Seifert, A. (2008) Understanding macrophysical outcomes of microphysical choices in simulations of shallow cumulus convection. *Journal of the Meteorological Society of Japan*, **86A**, 143–162.
- Tobias, S. M. and Marston, J. B. (2017) Three-dimensional rotating Couette flow via the generalised quasilinear approximation. *Journal of Fluid Mechanics*, **810**, 412–428. URL: https://www.cambridge.org/core/product/identifier/S0022112016007278/type/journal_article.
- VanZanten, M. C., Stevens, B., Nuijens, L., Siebesma, A. P., Ackerman, A. S., Burnet, F., Cheng, A., Couvreur, F., Jiang, H., Khairoutdinov, M., Kogan, Y., Lewellen, D. C., Mechem, D., Nakamura, K., Noda, A., Shipway, B. J., Slawinska, J., Wang, S. and Wyszogrodzki, A. (2011) Controls on precipitation and cloudiness in simulations of trade-wind cumulus as observed during RICO. *Journal of Advances in Modeling Earth Systems*, **3**.
- Young, G. S., Kristovich, D. A. R., Hjelmfelt, M. R. and Foster, R. C. (2002) Supplement to Rolls, Streets, Waves, and More. *Bulletin of the American Meteorological Society*, **83**, 1001–1001. URL: <http://journals.ametsoc.org/doi/abs/10.1175/BAMS-83-7-Young>.
- Zhdankin, V., Boldyrev, S., Perez, J. C. and Tobias, S. M. (2014) Energy dissipation in magnetohydrodynamic turbulence: Coherent structures or "nanoflares"? *Astrophysical Journal*, **795**.